


Enhanced spin state readout of nitrogen-vacancy centers in diamond using infrared fluorescence

I. Meirzada ¹, S. A. Wolf^{1,2}, A. Naiman^{1,2}, U. Levy^{2,3}, and N. Bar-Gill^{1,2,3,*}

¹*The Racah Institute of Physics, The Hebrew University of Jerusalem, Jerusalem 91904, Israel*

²*The Center for Nanoscience and Nanotechnology, The Hebrew University of Jerusalem, Jerusalem 91904, Israel*

³*Department of Applied Physics, Rachel and Selim School of Engineering, Hebrew University, Jerusalem 91904, Israel*



(Received 6 June 2019; revised manuscript received 13 August 2019; published 27 September 2019)

Nitrogen-vacancy (NV) centers in diamond have been used in recent years for a wide range of applications, from nanoscale NMR to quantum computation. These applications depend strongly on the efficient readout of the NV center's spin state, which is currently limited. Here we suggest a method of reading the NV center's spin state, using the weak optical transition in the singlet manifold. We numerically calculate the number of photons collected from each spin state using this technique, and show that an order of magnitude enhancement in spin-readout signal-to-noise ratio is expected, making single-shot spin readout within reach. Thus, this method could lead to an order of magnitude enhancement in sensitivity for ubiquitous NV-based sensing applications, and remove a major obstacle from using NVs for quantum information processing.

DOI: [10.1103/PhysRevB.100.125436](https://doi.org/10.1103/PhysRevB.100.125436)

Effective quantum state readout is a crucial component of almost every quantum computation or sensing device, and extensive research in a variety of fields is directed at improving quantum state measurements and increasing readout fidelity [1–4]. The nitrogen-vacancy (NV) color center in diamond is a promising system for various quantum-based applications, such as quantum computation [5] and sensitive measurements [6–11], due to its unique optical and spin properties. Nevertheless, a fast and high-fidelity spin-state readout for the NV center is currently missing, and although extensive efforts have been invested in this context [3, 12–15], many repetitions of each measurement, cold temperatures, or long measurement times are still needed for each experiment.

This paper presents a promising approach for reading the NV's spin state, based on fluorescence measurements of the singlet infrared (IR) transition. We first recalculate the standard red fluorescence-based spin-state readout with recently published ionization and recombination rates of NV[−] and NV⁰ [16]. Next, we detail our proposed method of reading the NV center's spin state, using the weak fluorescence emitted in the singlet manifold, and calculate the expected signal-to-noise ratio (SNR) by numerically solving the relevant rate equations for both surface and bulk NVs. From these results, we find a regime of excitation parameters for which a significant increase in the NV's spin-state readout SNR is expected. Finally, we suggest using a photonic crystal cavity to increase the radiative coupling of the singlet transition and present the quality and Purcell factors, as well as the SNR expected using these structures coupled to a nanodiamond, a diamond membrane, and bulk diamond.

The negatively charged NV center consists of two adjacent lattice sites occupied by a nitrogen atom and a vacancy inside a diamond crystal. The electronic ground state of the NV

center is a spin triplet with a 2.87 GHz zero-field splitting between spin projections $m_s = 0$ and $m_s = \pm 1$. The electronic excited states contain a spin triplet with a strong radiative coupling and a spin singlet with a much weaker radiative coupling.

Figure 1 depicts a simplified energy level diagram of NV[−] and NV⁰, together with their main transitions. In the standard red fluorescence spin-readout scheme, an NV in the triplet ground states (³A₂) is excited to the triplet excited states (³E₂) using green light, and the red fluorescence during the decay back to the ground state is collected. The number of photons collected from each of the spin states dictates the SNR, which is defined under the shot noise limit assumption as

$$\text{SNR} = \frac{|N_0 - N_1|}{\sqrt{N_0 + N_1}}, \quad (1)$$

where N_i denotes the number of photons collected when the NV is initialized to its $m_s = |i\rangle$ state, where i can be 0 or 1. Note that as the SNR increases, reaching unity and beyond, spin projection noise becomes important for quantifying spin-readout fidelity (compared to shot noise). In this regime, the readout fidelity is defined as Fidelity = $\frac{1}{\sqrt{1 + \frac{2(N_1 + N_0)}{(N_1 - N_0)^2}}} =$

$$\frac{1}{\sqrt{1 + \frac{2}{\text{SNR}^2}}}.$$

We first calculate the spin-readout SNR using green excitation and red fluorescence detection, as a function of readout duration and excitation power for a confocal system, for both surface and bulk NVs, assuming perfect collection and detection efficiencies. In addition, fluorescence from NV⁰ is ignored, although it overlaps to some extent with the NV[−] fluorescence. The SNR is calculated numerically, using an eight-level model (based on the levels depicted in Fig. 1), over a wide range of parameters. The rate equations dictating the populations for Fig. 2, as well as for Fig. 3, are the following

*Corresponding author: bargill@phys.huji.ac.il

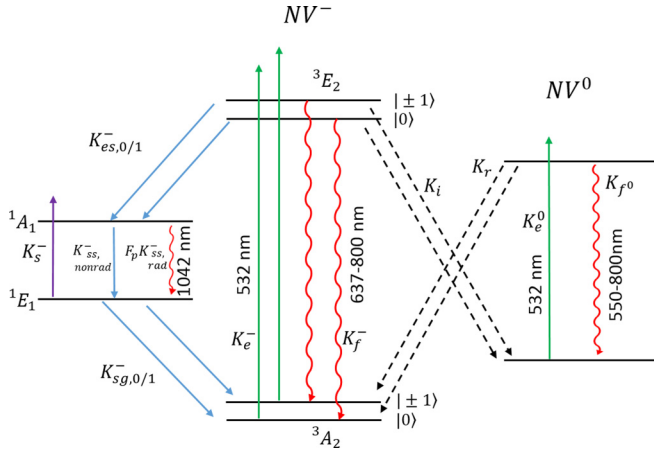


FIG. 1. Energy-level diagram and relevant transitions for the neutral and negatively charged NV center. Green excitation is depicted with green arrows, red fluorescence is depicted with downward red arrows, IR excitation and fluorescence are depicted with purple and red arrows, respectively, nonradiative decay is depicted with blue arrows, ionization and recombination transitions depicted with dashed black arrows.

[16–20]):

$$\begin{aligned}
 \dot{P}_{g,0}^- &= -K_e^- P_{g,0}^- + K_f^- P_{e,0}^- + K_{sg,0}^- P_{s,g}^- + \frac{1}{2}(K_{rG} + K_{rIR}) P_e^0, \\
 \dot{P}_{g,1}^- &= -K_e^- P_{g,1}^- + K_f^- P_{e,1}^- + K_{sg,1}^- P_{s,g}^- + \frac{1}{2}(K_{rG} + K_{rIR}) P_e^0, \\
 \dot{P}_{e,0}^- &= -(K_f^- + K_{es,0}^- + K_{iG} + K_{iIR}) P_{e,0}^- + K_e^- P_{g,0}^-, \\
 \dot{P}_{e,1}^- &= -(K_f^- + K_{es,1}^- + K_{iG} + K_{iIR}) P_{e,1}^- + K_e^- P_{g,1}^-, \\
 \dot{P}_{s,e} &= -(F_p K_{ss,rad}^- + K_{ss,nonrad}^-) P_{s,e} + K_{es,0}^- P_{e,0}^- \\
 &\quad + K_{es,1}^- P_{e,1}^- + K_s^- P_{s,g}, \\
 \dot{P}_{s,g} &= -(K_{sg,0}^- + K_{sg,1}^-) P_{s,g} - K_s^- P_{s,g} + (F_p K_{ss,rad}^- \\
 &\quad + K_{ss,nonrad}^-) P_{s,e}, \\
 \dot{P}_g^0 &= -K_e^0 P_g^0 + K_f^0 P_e^0 + (K_{iG} + K_{iIR})(P_{e,0}^- + P_{e,1}^-), \\
 \dot{P}_e^0 &= -(K_f^0 + K_{rG} + K_{rIR}) P_e^0 + K_e^0 P_g^0. \tag{2}
 \end{aligned}$$

In the above equations, $P_{g,0}^-$ and $P_{g,1}^-$ represent the population in the $m_s = 0$ and $m_s = \pm 1$ triplet ground states of the negatively charged NV, respectively, $P_{e,0}^-$ and $P_{e,1}^-$ represent the population in the $m_s = 0$ and $m_s = \pm 1$ triplet excited states of the negatively charged NV, respectively, P_g^0 and P_e^0 represent the populations of the neutral charge NV ground and excited states, respectively, and $P_{s,g}$ and $P_{s,e}$ represent the populations in the ground and excited singlet states of the negatively charged NV, respectively. K_e^- and K_e^0 represent the green laser-induced excitation rates of NV^- and NV^0 ground states to the excited states, respectively, K_s^- represents the IR laser-induced excitation rate from the ground singlet state to the excited singlet state, K_f^- and K_f^0 represent the fluorescence rate from the NV^- and NV^0 excited states to their ground states, respectively, $K_{ss,rad}^-$ and $K_{ss,nonrad}^-$ represent the radiative and nonradiative decay rates from the excited singlet state to the ground singlet state, respectively, F_p represents the

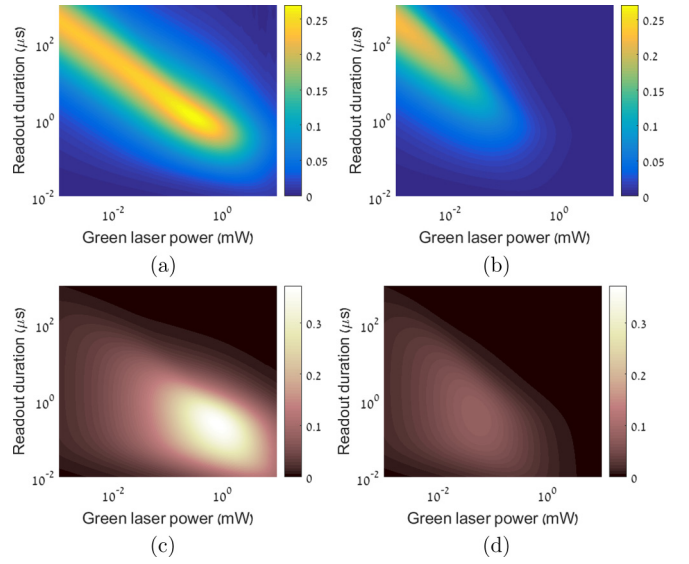


FIG. 2. SNR as a function of green excitation power and pulse duration for bulk (a), (c) and surface (b), (d) NVs, without (a), (b) and with (c), (d) time normalization. A big difference in the SNR between bulk and surface NVs is noticed due to the difference in ionization cross sections.

Purcell factor, which enhances the radiative rate, $K_{es,0}^-$ and $K_{es,1}^-$ represent the decay rates from the triplet excited states to the excited singlet state, respectively, $K_{sg,0}^-$ and $K_{sg,1}^-$ represent the decay rates from the ground singlet state to the NV^- $m_s = 0$ and $m_s = \pm 1$ triplet ground states, respectively, K_{iG} and K_{iIR} represent the green and IR excitation-induced ionization rates, respectively, and K_{rG} and K_{rIR} represent the green and IR excitation-induced recombination rates, respectively (see Ref. [16]).

Figure 2 illustrates the achievable red fluorescence spin-readout SNR, assuming 100% collection and perfect detection without external noise sources (such as dark counts). Figures 2(a) and 2(b) depict the absolute SNR, described in Eq. (1) for bulk and surface NVs, respectively, over a wide range of green excitation powers and readout durations. Figures 2(c) and 2(d) present the bulk [Fig. 2(c)] and surface [Fig. 2(d)] NV SNRs for the same power and duration regimes normalized by the square root of the pulse duration in μs . The significant difference in SNR between bulk and surface NVs stems from differences in the ionization cross section of the 3E_2 levels [16].

With the optimal parameters, the SNR rises slightly above 0.25 for bulk NVs and 0.22 for surface NVs. Thus, the red fluorescence spin readout demands a very high number of iterations before the spin state can be determined, even with perfect collection and detection, which limits the sensitivity and fidelity in NV-based sensing and quantum information applications.

We now detail the IR fluorescence-based spin-readout scheme. The pulsed sequence, depicted in Fig. 3(a), starts with a short and strong green laser pulse, exciting the NV from the ground state (3A_2) to the excited state (3E_2) and populating the singlet ground state (1E_1) of almost only $m_s = \pm 1$ polarized NVs. Next, a short delay (represented by τ) is introduced

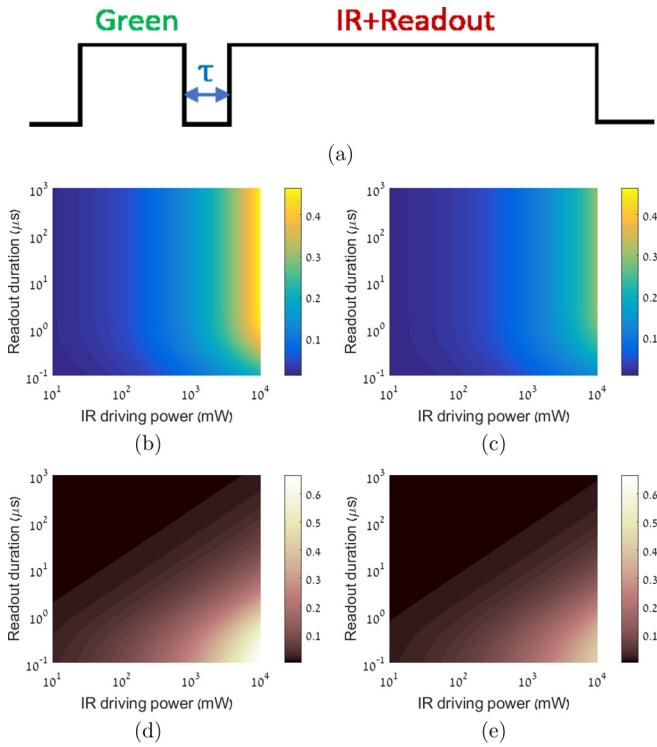


FIG. 3. IR fluorescence spin-state readout. (a) Pulse sequence for the IR fluorescence spin readout. (b)–(e) SNR as a function of IR excitation power and pulse duration for bulk NV (b), (d) and surface (c), (e) NVs, with (d), (e) and without (b), (c) normalization. Higher absolute and normalized SNR can be theoretically achieved compared to red fluorescence readout, for both bulk and surface NVs, using strong enough excitation.

to avoid undesired ionization from the excited triplet state, followed by a strong and long 980 nm pulse that excites the NV from the ground singlet state (1E_1) to the singlet excited state (1A_1) while collecting the emitted 1042-nm fluorescence. Due to the fact that the IR laser does not excite the triplet ground state, no mixing processes are expected, enabling a relatively long measurement. By carefully tuning the green laser pulse power and duration, the sequence can be repeated three times before significant mixing (via the singlet manifold or ionization/recombination processes) takes place, thus enhancing the signal.

Despite the poor radiative coupling between the 1A_1 and 1E_1 levels, the fast decay rate from the 1A_1 state [20] together with the relatively long shelving time in the 1E_1 state [21], enable a large number of cycles before the NV decays back to the 3A_2 ground state without risking photo-ionization, allowing for a large enough number of photons to be collected during a single measurement, for high enough excitation powers.

Figure 3 depicts the IR fluorescence spin-readout SNR as a function of IR laser power and pulse duration of bulk and surface NVs, with delay duration $\tau = 10$ ns (optimized with respect to the excited state lifetime). The laser power and pulse duration are scaled logarithmically to cover all of the relevant parameter space. Perfect collection and detection efficiencies are assumed for comparison with the results shown in Fig. 2. We neglect IR-induced ionization from the

singlet state, for which the cross section is currently unknown (but assumed to be small), and consider a radiative to non-radiative coupling ratio of 1/1000 [21]. Figures 3(b) and 3(c) present the calculated absolute SNR for bulk and surface NVs, showing an expected significant enhancement of the spin-state readout SNR compared to the red fluorescence spin-readout scheme for high enough IR power. In addition, in this scheme the SNR grows monotonically with readout duration due to the absence of spin mixing. Figures 3(d) and 3(e) present the calculated normalized SNR for bulk and surface NVs for the IR fluorescence method, showing that the normalized SNR can reach higher values than that of the red fluorescence spin-readout SNR for bulk and surface NVs, for strong excitation powers.

To further improve the spin-readout SNR shown in Fig. 3 while reducing the necessary IR excitation power, we need to overcome the weak fluorescence signal resulting from the nonradiative nature of the $^1A \rightarrow ^1E$ decay. Thus, we propose using optical/plasmonic antennas, hyperbolic metamaterials [12,22,23] or a photonic crystal cavity [24,25] to strengthen the radiative coupling between the 1A and 1E states and thus increase the singlet fluorescence signal.

Photonic crystal structures with small mode volumes ($V \approx (\lambda/n)^3$) and high quality factors (high frequency-to-bandwidth ratio in the resonator [26]) are now within reach [24,25], and together with the relatively narrow IR fluorescence spectral width, are expected to provide high Purcell factors, especially for nanodiamonds and diamond films, but also potentially for bulk diamonds.

The Purcell factor, an enhancement of the spontaneous emission rate from the excited state due to radiative coupling [26], depends on the quality factor and mode volume in the following way:

$$F_p = \frac{3}{4\pi^2} \left(\frac{\lambda}{n}\right)^3 \frac{Q}{V}, \quad (3)$$

where λ represents the wavelength, Q represents and quality factor, n represents the refractive index, and V represents the mode volume. In terms of the rate equations, the radiative part of the decay rate is multiplied by the Purcell factor. The fact that only approximately 0.1% of the decay results in photon emission holds great potential for enhancing the signal level and thus the SNR. In addition, the high emission directionality induced by a photonic crystal structure may dramatically increase the collection efficiency, and thus the number of photons detected.

Figure 4(a) describes schematically the suggested experimental system. Green and detuned IR lasers excite the triplet (3A_2) and singlet (1E_1) ground states, respectively, while Acousto-Optic Modulators (AOMs) modulate them. Two dichroic mirrors with proper cutoff wavelengths (533 nm—979 nm and 981 nm—1041 nm for the green and IR lasers, respectively) direct the lasers onto the objective and enable fluorescence collection on a single-photon counter module (SPCM), after the unwanted red fluorescence and reflected green and IR lasers are filtered out. The objective focuses the light onto the diamond sample, here illustrated as a nanodiamond, to reach the high intensity IR excitation needed for driving the singlet transition efficiently. Figures 4(b) and 4(c) illustrate the electric field's near-field and far-field energy

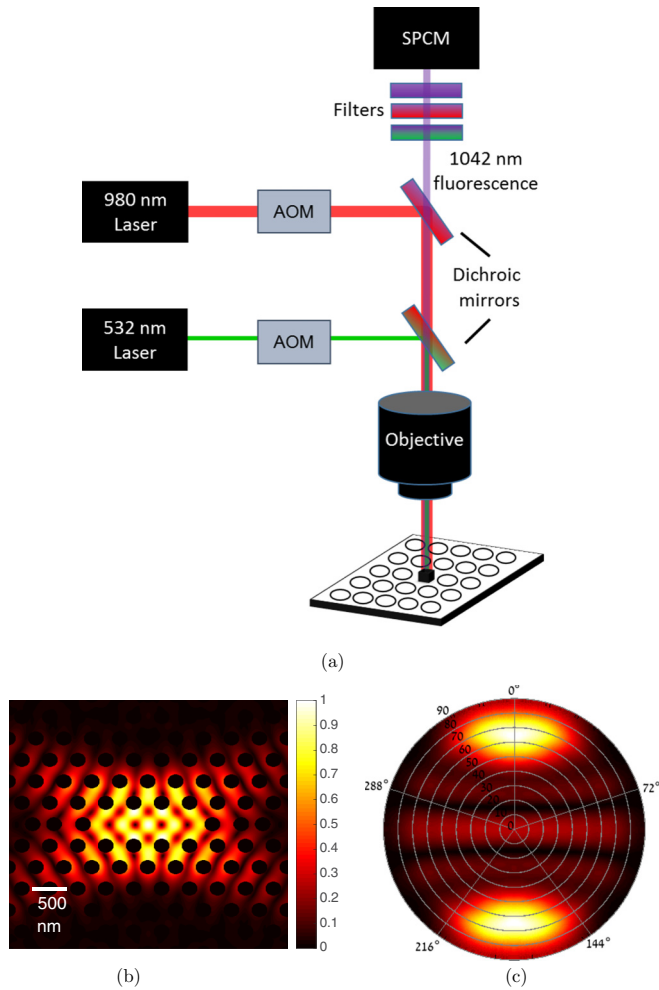


FIG. 4. Schematic drawing of the suggested experimental setup and electric field energy density of the photonic crystal structure. (a) Schematic drawing of the suggested experimental setup. Green and IR lasers are focused onto the diamond sample in a photonic crystal cavity structure using a high NA objective lens, while AOMs control the pulse sequencing. Fluorescence is then collected through the same objective and directed to an SPCM after filtering the red fluorescence and the green and IR photons reflected from the diamond's surface. (b) Photonic crystal structure and electric field near-field energy density. Three holes are shifted from each side to optimize Purcell factor. (c) Electric field far-field energy level density, showing highly directed emission from the cavity.

densities, as well as the photonic crystal cavity structure, optimized for nanodiamonds. The cavity structure is a 250-nm-thick silicone-nitride hexagonal PHC L3 cavity with five neighboring hole positions shifted, as described in Ref. [27]. For this structure, the refractive index is 2, the lattice constant, a , is 450 nm and hole radius is 125 nm, and the positions of the holes were shifted by $0.315a$, $0.35a$, $0.118a$, $0.205a$, and $0.284a$. The far-field energy density enables approximately 45% collection efficiency with numerical aperture of 0.95, while the near-field simulations predict a quality factor of about 2650 for this structure. Considering the small mode volume of this structure, $0.27(\frac{\lambda}{n})^3$, the resulting Purcell factor according to Eq. (3), which is manifested by K_s^- in Fig. 1, can

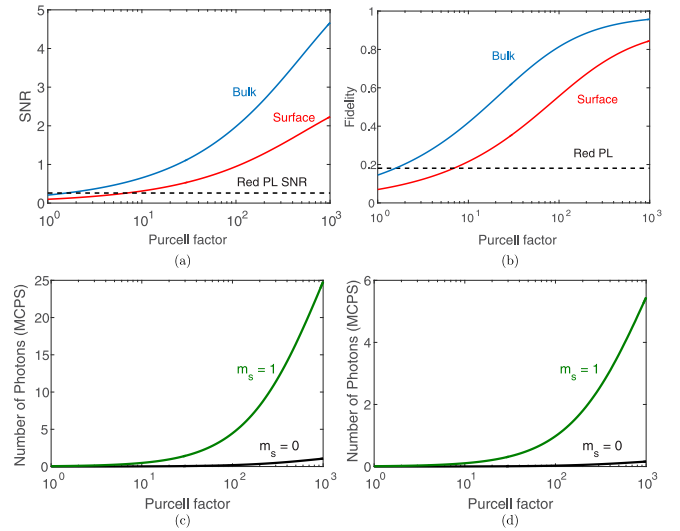


FIG. 5. Expected spin state SNR, fidelity and number of photons emitted as a function of Purcell factor under 1W excitation (inside the cavity), $1 \mu s$ readout duration and an optimized delay duration $\tau = 10$ ns. (a), (b) Spin-state readout SNR (a) and fidelity (b) for bulk (blue lined) and surface (red lines) NVs. The black line illustrates the highest SNR/fidelity possible for bulk NV using red fluorescence. (c), (d) Number of photons emitted during the singlet excitation for $m_s = 0$ (black lines) and $m_s = \pm 1$ (green lines) for bulk (c) and surface (d) NVs.

reach up to 2343, and thus significantly enhance the emission and the number of photons collected. Simulation over a wide range of wavelengths was performed to verify the existence of a single resonant mode in the spectral range of 500 nm–1100 nm, ensuring no enhancement of the radiative decay of the main transition ($3E$ to $3A$) [17]. Similar calculations for diamond membranes and bulk diamonds predict quality factors of up to 13 300 and 790 with mode volumes of $0.38(\frac{\lambda}{n})^3$ and $0.8(\frac{\lambda}{n})^3$, respectively, resulting in Purcell factors of up to 8355 for diamond membranes and 235 for bulk diamonds [17].

Figure 5 illustrates the expected spin-readout SNR and fidelity under 1W of IR excitation (inside the cavity) and a short readout duration ($1 \mu s$), as a function of Purcell factor for both surface (red line) and bulk (blue line) NVs. For this calculation, the Purcell factor was manifested by the radiative part of the rate K_s^- in Fig. 1. Based on the figure, the scheme provides a fivefold enhancement of the spin-readout SNR for a feasible Purcell factor of 40, which was already achieved for silicon-vacancy centers [28], and more than an order of magnitude enhancement for $F_p = 300$ and $F_p = 1000$ (which are significantly lower than the Purcell factors calculated for nanodiamonds and diamond membranes) for bulk and surface NVs, respectively, thus exceeding the single-shot readout threshold. The SNR can reach even higher values for readout duration $> 1 \mu s$ and higher excitation powers. Thus, the magnetic field sensitivity, which obeys the following relation [9,29]:

$$\eta \propto \delta B \sqrt{T} \propto \frac{1}{\text{SNR}}, \quad (4)$$

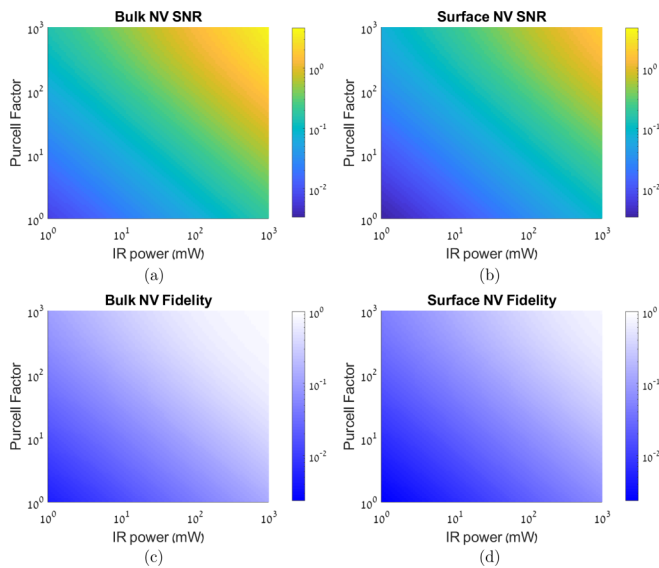


FIG. 6. Expected spin-readout SNR and fidelity as a function of Purcell factor and laser power. (a), (b) Expected spin state SNR for bulk (a) and surface (b) NV. (c), (d) Expected fidelity for (a) bulk and (b) surface NVs.

could be reduced by more than an order of magnitude as well (where T is the measurement time and δB is the minimum magnetic field that can be measured during this time).

Figures 5(b) and 5(c) present a calculation of the number of photons emitted from the $m_s = 0$ and $m_s = \pm 1$ spin states as a function of the Purcell factor for the same excitation power during the $1 \mu\text{s}$ readout duration, showing that a higher number of photons is expected to be emitted during the readout sequence, while the contrast between the two spin states is sustained. Figure 6 depicts the interplay between the IR excitation power and the Purcell factor in terms of their impact on the spin-readout SNR and fidelity. This is calculated both for bulk and surface NVs, over a wide range of parameters. Although the excitation power and Purcell factor change different parameters in the rate equations, low laser power can be compensated for by a higher Purcell factor and vice versa. Thus, a measurement with 100 mW of laser

excitation still produces a sixfold enhancement in the readout SNR for $F_p \approx 1000$, according to the simulation.

In this paper, we presented a spin-state readout scheme, based on the IR fluorescence emitted from the singlet manifold following IR excitation from the singlet ground state. Using numerical calculations, we showed that this scheme results in more than two orders of magnitude enhancement of the spin-readout SNR compared to the commonly used red fluorescence spin-readout scheme. The NV center's singlet states were hardly addressed in NV center research [21,30], and so far few references have described applications based on singlet excitation ([13,31]). Our readout method complements the absorption-based magnetometry presented in Ref. [31], as it generalizes it using the ${}^3E \rightarrow {}^3A$ transitions for low concentrations of defects, enabling this transition to be used in a wider range of applications based on single or few NVs as well as for high-density samples. Compared to other spin-readout methods presented in recent years—spin-to-charge readout [13,15], nuclear spin coupling [3], and resonant excitation [14]—our scheme could provide advantages in terms of measurement duration and the conditions required ($1 \mu\text{s}$ readout in room temperature vs 100 ms readout or ultracold systems). The significant SNR enhancement is expected to have a dramatic effect on nearly every NV-based application currently pursued: The fact that only a few repetitions are needed (instead of the usual tens of thousands) will result in significantly improved sensitivities in magnetometry and strain sensing, as they are measured with respect to experiment duration. In addition, the enhanced SNR may remove a major obstacle in using NVs for quantum information processing due to the importance of readout fidelity in this field. We are currently realizing this scheme experimentally, aiming to demonstrate enhanced spin-readout SNR and improved magnetic field sensitivity.

The authors thank D. Budker and J. Schloss for their insights and comments. This project has received funding from the European Research Council (ERC) under the European Union's Horizon 2020 research and innovation programme (Grant Agreement No. 714005). This work has been supported in part by the European Union Quantum Flagship project MetaboliQs, the European Union FET-Open project PATHOS, the Ministry of Science and Technology, Israel and the Israeli Innovation Authority.

-
- [1] M. D. Reed, L. DiCarlo, B. R. Johnson, L. Sun, D. I. Schuster, L. Frunzio, and R. J. Schoelkopf, *Phys. Rev. Lett.* **105**, 173601 (2010).
- [2] A. H. Myerson, D. J. Szwer, S. C. Webster, D. T. C. Allcock, M. J. Curtis, G. Imreh, J. A. Sherman, D. N. Stacey, A. M. Steane, and D. M. Lucas, *Phys. Rev. Lett.* **100**, 200502 (2008).
- [3] M. Steiner, P. Neumann, J. Beck, F. Jelezko, and J. Wrachtrup, *Phys. Rev. B* **81**, 035205 (2010).
- [4] A. Morello, J. J. Pla, F. A. Zwanenburg, K. W. Chan, K. Y. Tan, H. Huebl, M. Möttönen, C. D. Nugroho, C. Yang, J. A. van Donkelaar, A. D. C. Alves, D. N. Jamieson, C. C. Escott, L. C. L. Hollenberg, R. G. Clark, and A. S. Dzurak, *Nature* **467**, 687 (2010).
- [5] G. D. Fuchs, G. Burkard, P. V. Klimov, and D. D. Awschalom, *Nat. Phys.* **7**, 789 (2011).
- [6] H. Clevenson, M. E. Trusheim, C. Teale, T. Schröder, D. Braje, and D. Englund, *Nat. Phys.* **11**, 393 (2015).
- [7] V. M. Acosta, E. Bauch, A. Jarmola, L. J. Zipp, M. P. Ledbetter, and D. Budker, *Appl. Phys. Lett.* **97**, 174104 (2010).
- [8] F. Dolde, H. Fedder, M. W. Doherty, T. Nöbauer, F. Rempp, G. Balasubramanian, T. Wolf, F. Reinhard, L. C. L. Hollenberg, F. Jelezko, and J. Wrachtrup, *Nat. Phys.* **7**, 459 (2011).
- [9] J. M. Taylor, P. Cappellaro, L. Childress, L. Jiang, D. Budker, P. R. Hemmer, A. Yacoby, R. Walsworth, and M. D. Lukin, *Nat. Phys.* **4**, 810 (2008).

- [10] M. Loretz, S. Pezzagna, J. Meijer, and C. L. Degen, *Appl. Phys. Lett.* **104**, 033102 (2014).
- [11] M. E. Trusheim and D. Englund, *New J. Phys.* **18**, 123023 (2016).
- [12] S. A. Wolf, I. Rosenberg, R. Rapaport, and N. Bar-Gill, *Phys. Rev. B* **92**, 235410 (2015).
- [13] B. J. Shields, Q. P. Unterreithmeier, N. P. de Leon, H. Park, and M. D. Lukin, *Phys. Rev. Lett.* **114**, 136402 (2015).
- [14] L. Robledo, L. Childress, H. Bernien, B. Hensen, P. F. A. Alkemade, and R. Hanson, *Nature* **477**, 574 (2011).
- [15] D. A. Hopper, R. R. Grote, A. L. Exarhos, and L. C. Bassett, *Phys. Rev. B* **94**, 241201(R) (2016).
- [16] I. Meirzada, Y. Hovav, S. A. Wolf, and N. Bar-Gill, *Phys. Rev. B* **98**, 245411 (2018).
- [17] See Supplemental Material at <http://link.aps.org/supplemental/10.1103/PhysRevB.100.125436> for more information regarding rate equations and photonic crystal properties.
- [18] L. Robledo, H. Bernien, T. v. d. Sar, and R. Hanson, *New J. Phys.* **13**, 025013 (2011).
- [19] J.-P. Tetienne, L. Rondin, P. Spinicelli, M. Chipaux, T. Debuisschert, J.-F. Roch, and V. Jacques, *New J. Phys.* **14**, 103033 (2012).
- [20] R. Ulbricht and Z.-H. Loh, *Phys. Rev. B* **98**, 094309 (2018).
- [21] V. M. Acosta, A. Jarmola, E. Bauch, and D. Budker, *Phys. Rev. B* **82**, 201202(R) (2010).
- [22] N. Livneh, A. Strauss, I. Schwarz, I. Rosenberg, A. Zimran, S. Yochelis, G. Chen, U. Banin, Y. Paltiel, and R. Rapaport, *Nano Lett.* **11**, 1630 (2011).
- [23] M. G. Harats, N. Livneh, G. Zaiats, S. Yochelis, Y. Paltiel, E. Lifshitz, and R. Rapaport, *Nano Lett.* **14**, 5766 (2014).
- [24] N. H. Wan, S. Mouradian, and D. Englund, *Appl. Phys. Lett.* **112**, 141102 (2018).
- [25] S. Mouradian, N. H. Wan, T. Schröder, and D. Englund, *Appl. Phys. Lett.* **111**, 021103 (2017).
- [26] S. Haroche and D. Kleppner, *Phys. Today* **42**(1), 24 (1989).
- [27] M. Minkov and V. Savona, *Sci. Rep.* **4**, 5124 (2014).
- [28] J. L. Zhang, S. Sun, M. J. Burek, C. Dory, Y.-K. Tzeng, K. A. Fischer, Y. Kelaita, K. G. Lagoudakis, M. Radulaski, Z.-X. Shen, N. A. Melosh, S. Chu, M. Lončar, and J. Vučković, *Nano Lett.* **18**, 1360 (2018).
- [29] L. Pham, Magnetic field sensing with nitrogen-vacancy color centers in diamond, Ph.D. thesis, Harvard University (2013).
- [30] P. Kehayias, M. W. Doherty, D. English, R. Fischer, A. Jarmola, K. Jensen, N. Leefer, P. Hemmer, N. B. Manson, and D. Budker, *Phys. Rev. B* **88**, 165202 (2013).
- [31] Y. Dumeige, M. Chipaux, V. Jacques, F. Treussart, J.-F. Roch, T. Debuisschert, V. M. Acosta, A. Jarmola, K. Jensen, P. Kehayias, and D. Budker, *Phys. Rev. B* **87**, 155202 (2013).